



Mass spectrometry imaging to explore molecular heterogeneity in cell culture

Tanja Bien^{a,b,1} , Krischan Koerfer^{c,d,1} , Jan Schwenzfeier^a , Klaus Dreisewerd^{a,b} , and Jens Soltwisch^{a,b,2}

Edited by Carol Robinson, University of Oxford, Oxford, United Kingdom; received August 4, 2021; accepted May 13, 2022

Molecular analysis on the single-cell level represents a rapidly growing field in the life sciences. While bulk analysis from a pool of cells provides a general molecular profile, it is blind to heterogeneities between individual cells. This heterogeneity, however, is an inherent property of every cell population. Its analysis is fundamental to understanding the development, function, and role of specific cells of the same genotype that display different phenotypical properties. Single-cell mass spectrometry (MS) aims to provide broad molecular information for a significantly large number of cells to help decipher cellular heterogeneity using statistical analysis. Here, we present a sensitive approach to single-cell MS based on high-resolution MALDI-2-MS imaging in combination with MALDI-compatible staining and use of optical microscopy. Our approach allowed analyzing large amounts of unperturbed cells directly from the growth chamber. Confident coregistration of both modalities enabled a reliable compilation of single-cell mass spectra and a straightforward inclusion of optical as well as mass spectrometric features in the interpretation of data. The resulting multimodal datasets permit the use of various statistical methods like machine learning–driven classification and multivariate analysis based on molecular profile and establish a direct connection of MS data with microscopy information of individual cells. Displaying data in the form of histograms for individual signal intensities helps to investigate heterogeneous expression of specific lipids within the cell culture and to identify subpopulations intuitively. Ultimately, t-MALDI-2-MSI measurements at 2- μm pixel sizes deliver a glimpse of intracellular lipid distributions and reveal molecular profiles for subcellular domains.

single-cell mass spectrometry | t-MALDI-2-MSI | cellular heterogeneity | lipidomics

To understand the function and role of a specific cell type in a biological system, in-depth information about its molecular composition is often of paramount importance. Typically, this information is derived from ensemble populations, such as cell cultures or extracted and pooled cells of a certain phenotype. However, individual cells of the same cell type can display different morphological and chemical phenotypes and cellular heterogeneity on both a morphological and a molecular level is ubiquitous in any population of cells (1, 2). This cell-to-cell heterogeneity can have several origins, for example a varying cellular environment, the status within the cell cycle, age and differentiation, genetic differences resulting from mutations (3, 4), or also stochastic events in gene expression (5). Deciphering chemical heterogeneity on a single-cell level can help to understand the function of cells of a particular type and also how they specifically respond to therapeutics or other stimuli (6, 7). To address these differences between individual cells, molecular analysis on the single-cell level is necessary.

Fluorescence-based microscopic techniques are well-established and widely applied for the identification and quantification of targeted proteins, glycosphingolipids, and, in some cases, secondary metabolites from single cells using specific stains and dyes. On the same basis, fluorescence-activated cell sorting (FACS) can be used to identify and sort cells based on a specific molecular marker for consecutive mass spectrometric analysis of certain groups of cells (8). The main advantages of fluorescence detection include a high sensitivity and a generally high specificity as well as its nondestructive nature and high-throughput capabilities (9). However, fluorescent tagging is highly targeted and numerous important classes of biomolecules, in particular lipids, such as, for example, phospholipids and sterols, are not amenable to the technique due to the lack of specific chromophores. FACS as well as laser microdissection can also be used to separate cells for single-cell RNA sequencing. This technique is able to profile the whole transcriptome of thousands of individual cells simultaneously and enables understanding the expression of genes at the single-cell level, deciphering their heterogeneity within a cell population, and revealing subpopulations within a cell culture (10, 11).

Similar to RNA sequencing, single-cell mass spectrometry (single-cell MS) can provide for an untargeted and label-free approach based on molecular analysis. Here, complete

Significance

Single-cell mass spectrometry (MS) provides molecular information on a cellular level and enables the analysis of cellular heterogeneity. In this study, we demonstrate an approach to single-cell MS that utilizes a combination of state-of-the-art MS imaging to generate molecular information with compatible staining and slide-scanning microscopy for segmentation of individual cells. Both modalities are coregistered to generate single-cell mass spectra. Using statistical tools and machine learning, single-cell MS data are used to identify subclasses within the cell culture. On the level of individual lipids, molecular heterogeneity is displayed using histograms and coregistration of MS imaging and microscopy links of both modalities in data analysis. Beyond cellular resolution, the use of 2- μm pixels enables the molecular investigation of intracellular domains.

Author contributions: T.B., K.K., and J. Soltwisch designed research; T.B., K.K., J. Schwenzfeier, and J. Soltwisch performed research; T.B., K.K., J. Schwenzfeier, and J. Soltwisch analyzed data; and T.B., K.K., J. Schwenzfeier, K.D., and J. Soltwisch wrote the paper.

The authors declare no competing interest.

This article is a PNAS Direct Submission.

Copyright © 2022 the Author(s). Published by PNAS. This article is distributed under [Creative Commons Attribution-NonCommercial-NoDerivatives License 4.0 \(CC BY-NC-ND\)](https://creativecommons.org/licenses/by-nc-nd/4.0/).

¹T.B. and K.K. contributed equally to this work.

²To whom correspondence may be addressed. Email: jenssol@uni-muenster.de.

This article contains supporting information online at [http://www.pnas.org/lookup/suppl/doi:10.1073/pnas.2114365119/-/DCSupplemental](https://www.pnas.org/lookup/suppl/doi:10.1073/pnas.2114365119/-/DCSupplemental).

Published July 11, 2022.

molecular classes like proteins, metabolites and lipids can be investigated on the single-cell level (12–14). In this context, lipids are a highly interesting group of analytes (15). Overall, the lipid composition of a cell impacts many biological processes and it also strongly depends on microenvironmental cues, the cell cycle, and even cell states (16–18). Naturally, lipid composition therefore often expresses heterogeneity even in cell populations of the same type. MS is the core analytical technique in lipidomic applications. In particular, the combination of chromatography and electrospray ionization (ESI) is a routine tool for deciphering the lipid composition from a pool of cells and occasionally even at the single-cell level (19, 20). However, because of the limited sample volumes, single-cell metabolomics/lipidomics remains challenging (21). A typical eukaryotic cell, for example, contains only 4.2 pL of volume, and even highly abundant lipids such as cholesterol are then present at low-femtomole levels only (22).

Because of its capability to effectively generate intact molecular ions from minute sample volumes, matrix-assisted laser desorption ionization (MALDI) has become increasingly popular in single-cell MS. In general, two modes of operation have been described. In profiling approaches, single cells are isolated on a target plate and the laser is focused to cell-specific coordinates. Typically, the laser spot diameter used in these experiments exceeds that of the target cells and the cell content is completely sampled within repetitive laser shots. In cell profiling, the target coordinates are either predefined by microarrays (13, 23–28) or individual cells are randomly dispersed and deposited on a surface like a glass slide and located using an optical microscope (29, 30). This approach allows for the analysis of thousands of cells in a single experiment and a straightforward combination with immunocytochemistry (14, 31). To avoid cross-contamination between single cells in a profiling experiment, however, cells from culture or tissue have to be separated and isolated. This isolation of the cells may limit the investigation of long-range cellular outgrowth and changes related to cell-to-cell signaling (32).

In contrast to the profiling approach, a typical MALDI-MS imaging (MSI) experiment probes the entire sample surface in a regular raster of pixels, independent of the cell coordinates. Cells in the investigated area can either also be separated by microarrays (33) or are directly grown on the sample slide. For single-cell analysis, data from all pixels that are specific to an individual cell are combined to yield single-cell mass spectra either in a “manual” fashion (16) or by coregistering the pixel position to microscopic images of the cells in the sampled area (7, 34). For this, optical images of cells and tissue are recorded pre- and/or post-MALDI-MSI analysis and MALDI ablation marks and/or fiducial markers that are placed off the region of interest are used for coregistration (34, 35). Although dedicated algorithms have been developed to segment and identify individual cells in the microscopy images with high accuracy, a precise coregistration is often described as a bottleneck, especially for densely grown cell cultures or tissue samples. Next to enabling single-cell MS analysis, the coregistration allows for a direct comparison of MS data with the histological assessment of cells based on light optical modalities, such as fluorescence microscopy or morphometric analysis. These techniques typically exceed the abilities of MALDI-MSI with regard to spatial resolution considerably (35, 36).

While in cell-profiling mode the isolation of cells permits the use of relatively large laser spot sizes, single-cell analysis of unperturbed cell culture using MALDI-MSI requires the use of small pixels. To avoid intermixing of information from neighboring cells, generally, the pixel size should be in the range of

the cellular dimensions, namely within 10 μm and below, a value now in reach on some commercially available MALDI-MSI instruments. More specialized ion sources can already reach a pixel size of 1 to 2 μm for the analysis of cultured cells (37–39).

To increase the analytical sensitivity for numerous classes of lipids and further metabolites, a laser-based postionization strategy, named MALDI-2, can be used (40–42). The technique reduces ion suppression effects, typical in MALDI-MSI of lipids (43), and increases ion yields by up to three orders of magnitude for a number of lipid classes. MALDI-2 thereby enhances molecular coverage and chemical depth significantly, especially for minute sample amounts. Combining the method with transmission-mode (*t*-MALDI), we have demonstrated MALDI-MSI analysis with pixel sizes of 1 to 2 μm for cell cultures (39, 44). Next to improvements in irradiation geometry and ion boost, these high spatial resolution experiments call for precise and optimized sample preparation. Particular care has to be taken to avoid changes in cell morphology, diffusion of analyte molecules, and chemical alteration. We have recently reported an optimized protocol including MALDI-compatible formalin fixation, washing, drying, and matrix application steps for the analysis of cell culture (44).

Here, we present a workflow to investigate intra- and intercellular heterogeneity in cultured cells by combining MALDI-MSI and optical microscopy. Data from both modalities are spatially correlated with high accuracy using simple overlay algorithms fed with data from specific fluorescence staining and bright-field microscopy, on the one hand, and matching information derived from selected MSI channels on the other, thereby omitting the use of fiducial markers or coregistration based on ablation marks (34, 35). High-fidelity coregistration allows for the compilation of an individual mass spectrum for each individual cell and enables statistical analysis of cell heterogeneity based on individual single-cell mass spectra. This cellular heterogeneity can, in turn, be directly correlated and compared with phenotypical observations for the same cells based on optical microscopy. We further demonstrate the use of machine learning (ML) to classify specific groups of cells based on their molecular profile. The presented methods for data acquisition and processing were validated using *t*-MALDI-2-MSI with a pixel size of 2 μm to investigate the influence of spatial resolution on coregistration and the compilation of single-cell mass spectra. In two proof-of-concept applications, 1) a cocultivation of Vero-B4 and Caki-2 cells was used to demonstrate the analytical capabilities of the method regarding classification of different cell types and visualization of intercellular heterogeneity, and 2) changes in lipid profile were monitored during the differentiation of THP-1 monocytes into macrophages. Both studies were carried out at 8- μm pixel size using MALDI-2-MSI on a modified timsTOF fleX (Bruker Daltonics) instrument. At high spatial resolution, the use of single-pixel rather than single-cell mass spectra for statistical analysis furthermore allowed for the molecular analysis of intracellular structure.

Results and Discussion

Single-cell MS relies on the production of meaningful mass spectrometric data and their confident and unambiguous correlation to an individual cell. In MALDI-MSI approaches, this correlation is often hampered by the available spatial resolution because a pixel size exceeding 10 to 15 μm often does not allow for an unequivocal assignment of every recorded pixel to a specific single cell. In contrast, histological techniques readily enable the identification and segmentation of cells in cultures and tissue. In combination with MALDI-MSI, most commonly

the histological analysis is performed after the MSI step and includes washing of the matrix, staining, and drying. However, these protocols may lead to skewing or regionalized image warping between MSI and histology, especially in the analysis of fresh-frozen tissue sections (45). These effects can necessitate cumbersome additional work steps that may include the generation of microscopic images pre- and post-MALDI-MSI, the use of overlay of MALDI-MS ablation marks, or rely on fiducial markers placed off the tissue region of interest (34, 35). To determine the spatial correspondence between MSI and histological data with high fidelity, registration algorithms exist, which use rigid registration of images, binarized by threshold values, to separate tissue and background by total ion intensities (46) or nonlinear and linear dimensionality reduction techniques for summarizing MSI datasets like t-SNE or *k*-means clustering (47, 48).

In order to simplify the coregistration between MSI and histological data, we minimized adverse effects during sample handling. Amending our previously developed optimized sample preparation protocol for MALDI-MSI of cultured cells (44), Hoechst stain 33342 (Hoechst from here on) and wheat germ agglutinin (WGA) were used to stain cell nuclei and cellular membranes, respectively. Notably, with regard to the chemical integrity in the lipid domain, both stains are fully compatible with MALDI-MSI of lipids. Advantageously, this allows recording histological data prior to the dry sublimation-based application of the MALDI matrix omitting any tissue warping induced by washing or wetting and subsequent drying in-between the two optical modalities. For coregistration, *m/z* channels were selected to display homogeneous signal intensity in all cells while being absent from the background. For all investigated cell lines, the prominent signal at *m/z* 577.520, tentatively assigned to diacylglycerol [DAG(34:1)–H₂O+H]⁺, was chosen. This *m/z* value most probably combines the result of in-source fragmentation of a number of lipid species like phosphatidylcholine PC(34:1), phosphatidylethanolamine PE(34:1), and phosphatidylserine PS(34:1) (*SI Appendix*, Fig. S1). It shows low intra- and intercellular heterogeneity and is, therefore, detected ubiquitously throughout all investigated cells. These preconditions permit a simple coregistration based on two-dimensional pixel correlation between binarized MSI and microscopy data (see *Materials and Methods* and *SI Appendix*, Fig. S2 for details). The global information of both MALDI and microscopy images is used to determine three parameters (*x* and *y* positions and angle of rotation) for the coregistration. Consequently, the approach does not account for tissue warping but, given undeformed images, it is more precise and more robust to local noise or overfitting than techniques that use all affine or even nonrigid transformations. The capacity of the approach is demonstrated in Fig. 1 and *SI Appendix*, Figs. S2 and S3, showing a high correlation between the WGA stain (Fig. 1*A*) and the t-MALDI-2-MSI data recorded from a Vero-B4 monoculture at a pixel size of 2 μ m (Fig. 1*B*).

Furthermore, histological images based on Hoechst and WGA stains enabled a segmentation of the data into background and areas associated with individual cells (see *Materials and Methods* for details). This segmentation is displayed using outlines around each cell in Fig. 1*C* overlaid with the mass spectrometric data, again demonstrating the high fidelity of coregistration. The combination of coregistration and segmentation now enables applying the workflow for single-cell data extraction and further processing, as visualized in Fig. 2. It allows generating sum mass spectra for each segmented area, which include all MSI pixels identified to allocate to the respective individual cell. To avoid ambiguity in the resulting single-

cell mass spectra, all pixels allocated to more than one cell are discarded from the sum. Resulting data now contain the spatial information and position of each cell from the microscopy modality, on the one hand, and a single-cell mass spectrum from the MSI measurement, on the other. As outlined in Fig. 2, this allows for the application of a wide range of statistical tools or analysis using ML based on MS data on the single-cell level and a direct correlation of the results with the optical modality.

To evaluate a coregistration for pixel sizes larger than 2 μ m, as commonly available in commercially available imaging mass spectrometers, we artificially upsampled the same MALDI-MSI datasets by combining neighboring pixels. Considering the original dataset as ground truth, correlation results for pixel sizes of 4, 8, 16, and 32 μ m demonstrate the suitability of intensity-based coregistration for modalities even at significantly larger pixel sizes (see *SI Appendix*, Fig. S4*A* and Table S1 for the 32- μ m pixel overlay). Whereas the MSI analysis of a large number of cells is accelerated by increasing the employed pixel size, the discarding of ambiguous pixels that allocate with more than one cell sets a practical limit to this value. This limit will strongly depend on the size of the cell line under investigation and its degree of (sub)confluence of the culture's growth. To estimate this pixel size effect, a grid of varying theoretical pixel sizes can be overlaid with the optical image of the cell culture. Applied to our culture of Vero-B4 cells, at 2- μ m pixel size, more than 80% of all pixels completely fall within the area of a single cell and only 2.3% touch more than one cell. At 16- μ m pixel size, most pixels (78.3%) only partially cover the cell surfaces and 17.4% have to be discarded. Next, to a summary of this effect in Table 1, it is also demonstrated using pie charts in *SI Appendix*, Fig. S4. Based on these data available from microscopic images, it is possible to predefine a pixel discard rate acceptable for the application at hand and derive the required pixel size for MALDI-MSI. For all further experiments, a discard rate of 10% was chosen that requires maximum pixel sizes of 8 μ m and permits a data acquisition rate of about 4.6 mm²/h at 20 pixels per second when performed on the timsTOF fleX MALDI-2 instrument.

Coculturing and Classification. While both computer-aided and manual cell sorting based on morphological phenotype or fluorescence labeling are well-established tools in histology, it is usually time-consuming and/or computationally expensive (49). Additionally, the methods may miss molecular phenotypes that are not targeted by the used fluorescent tag or that are not reflected in morphological differences. Classification based on single-cell mass spectra as generated by MSI, on the other hand, can utilize hundreds of different *m/z* channels to identify these "molecular phenotypes" and directly link them to histological data.

To demonstrate the analytical potential for classifying cells based on their single-cell mass spectra, we chose a coculture of two different epithelial kidney cell lines, namely Vero-B4 and Caki-2, as a model system. Additionally, the MSI-based classification results of the cell lines can be compared with state-of-the-art optical classification techniques. Using this model system, we conducted MALDI-MSI on areas containing between 300 and 800 cells and compiled a list of the most prominent peaks in the mass spectrometric datasets (about 500 peaks) of both monocultures and of the coculture of both cell lines (see *Materials and Methods* and *SI Appendix*, *Methods* for details). Single-cell mass spectra from the experiments were reduced to centroid data containing only the selected *m/z* channels and normalized to the total ion count (TIC)

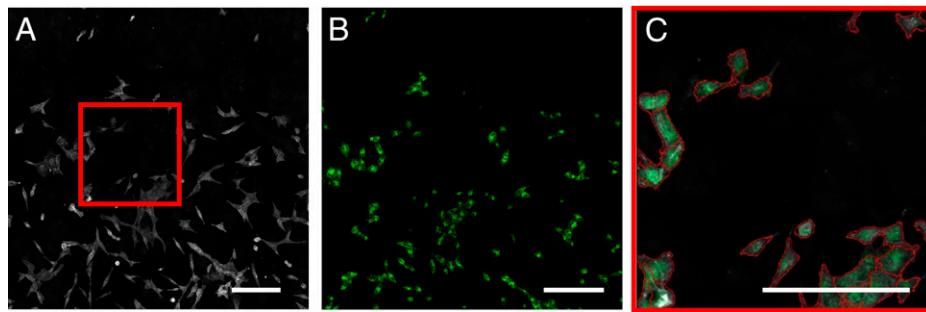


Fig. 1. (A and B) Vero-B4 cell culture visualized in (A) a fluorescence microscopy image using WGA stain and (B) the corresponding ion signal intensity distribution of $[DAG(34:1)-H_2O+H]^+$ registered at m/z 577.520 using t-MALDI-2-MSI. (C) Zoom-in of t-MALDI-2-MS image overlaid with the result of a single-cell segmentation based on microscopy data (orange outlines). (Scale bars, 200 μm .)

of the reduced spectra. This data reduction and normalization ensured easy comparability across the different measurements and reduced computational cost. Resulting datasets were used in two complementary classification approaches based on ML (in the form of a support vector machine; SVM) and multivariate statistical analysis (principal-component analysis; PCA), respectively.

For the ML approach, monocultured cells were used as labeled training data. The dataset contained 722 Vero-B4 and 312 Caki-2 cells and was randomly partitioned into five

groups of equal size for a fivefold cross-validation. A linear SVM classifier was trained on all five training- and test-set combinations and achieved an average classification accuracy of 99.9% with only misclassifying a single cell in the entire dataset. Our data suggest that training sets consisting of a few hundred cells are sufficient for classification with high confidence. Subsequently, the SVM was retrained on the complete datasets of the monocultures and then used to predict the cell types of the coculture.

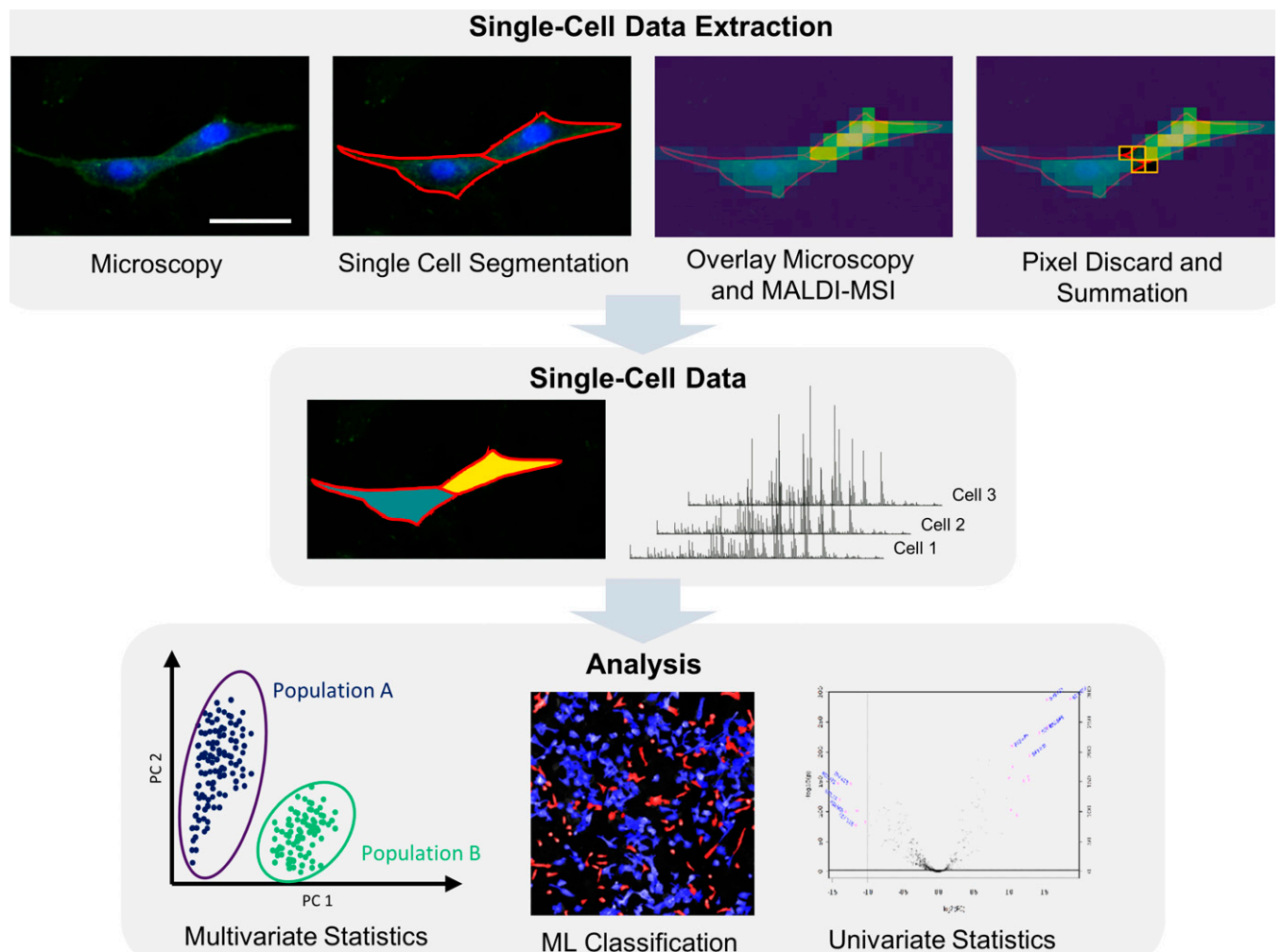


Fig. 2. Illustration of the workflow for single-cell analysis by the combination of microscopy and high-resolution MALDI-MSI. Segmentation of the microscopy data are followed by a pixelwise coregistration with MALDI-MSI data. Mass spectra from pixels associated with a specific cell are summed to single-cell mass spectra and are considered as the absolute single-cell intensities. Pixels that are associated with more than one cell are discarded. Single-cell data can subsequently be used for ML classification or any desired method of statistical data analysis. (Scale bar, 50 μm .)

Table 1. Impact of MALDI pixel-size on full or partial coverage of a single cell by the pixel area and the possibility of ambiguous coverage of multiple cells

	2 μ m	4 μ m	8 μ m	16 μ m	32 μ m
One cell, 100%	83.5	57.9	26.6	4.3	0.0
One cell, 50 to 99%	9.5	19.0	28.0	24.3	9.1
One cell, 1 to 49%	4.8	17.3	34.6	54.0	61.9
Two cells (pixel discarded)	2.3	5.8	10.7	17.4	29.0

Percentage of pixels allocated with Vero-B4 cells in a t-MALDI-2-MSI measurement where the full pixel covers a single cell (100%), more than half of the pixel area covers a single cell (50 to 99%), less than half of the pixel area (1 to 49%) covers a single cell, and the pixel area partially covers two cells and needs to be discarded from analysis. Data are shown for the 2- μ m pixel size measurements and the same measurements with artificially upscaled pixel sizes of 4, 8, 16, and 32 μ m. Pixels not hitting a cell based on segmentation results are excluded.

An overlay of Hoechst and WGA staining of the coculture is displayed in Fig. 3*A*. By using the established coregistration with the microscopy data, the results of the classification were used to label the cells accordingly in the bright-field image (Fig. 3*B*). To compare these results with state-of-the-art histological methods, artificial intelligence (AI)-driven classification provided by Olympus deep-learning solution (50) was applied to the same set of cells. It differentiates cells based on Hoechst and WGA fluorescence as well as bright-field microscopy and can provide high fidelity for cells with distinctively different phenotypes (Fig. 3*C*). While in general the microscopy-based classification results are comparable to the MSI-based classification, a number of cells are assigned differently by the two methods (compare the white arrows in Fig. 3*B* and *C* for examples). In general, Caki-2 cells are larger and rounder, while the typical Vero-B4 cells are smaller with irregularly spreading edges. Most discrepancies between the two classifications are found where the cells' morphology cannot be clearly placed in either category.

To investigate the robustness and fidelity of the assignment produced by the SVM, the method was applied to a biological replicate of the coculture sample system. To provide an independent ground truth, Caki-2 cells were stained with a live-cell dye (CellTracker Deep Red) prior to combining both cell lines. This allows for an unambiguous identification of the respective cell type in the coculture based on fluorescence microscopy. *SI Appendix, Fig. S5* shows the stained image and Fig. 3*E* shows the resulting classification of cells as Caki-2 in green (see *SI Appendix, Methods* for details). Applying the SVM trained on the previous dataset, Caki-2 and Vero-B4 cells are identified with a recall of 97 and 75%, respectively, resulting in a total accuracy of 79% (compare Fig. 3*D* and *G*). While precision for identification of Vero-B4 is high (99%), a comparably low recall for these cells in combination with a substantially higher number of Vero-B4 than Caki-2 cells in the sample, in turn, leads to a rather low precision in identifying Caki-2 cells of 45% from this strictly binary system. From a biological perspective, these variances may be explained by molecular variation in the cells derived from independently produced cell cultures (biological replicates from the same stock culture) at differing culture times and passage. While the cancer-derived Caki-2 cells are relatively stable with increasing numbers of passages, morphological and molecular changes have been reported for noncancerous cell lines, such as Vero-B4, with increasing numbers of passages. Training the SVM on monocultures of the same passage of cell lines leads to an accurate identification in the coculture of 91 and 92% recall with a precision of 74 and 98% for Caki-2 and Vero-B4 cells, respectively, and a high total accuracy of 92% (Fig. 3*F* and *H*). While this underlines the necessity for

an optimal training set for the SVM, it also highlights the specificity of the method for a certain molecular state of the investigated cells. It is to be expected that training the SVM on a combination of different biological replicates of different passages would result in an improved generalization of the SVM, increasing the accuracy to classify a specific cell type when compared with other cells, while, at the same time, losing sensitivity for heterogeneities between different passages and culturing times.

To visualize the separation of the two cell types in a two-dimensional plane, we performed a PCA. Applied to the combined datasets of two separately acquired monocultures, the PCA revealed that 24% of the cell-to-cell variability is explained by the first two PCs and that the two cell types split into relatively distinct clusters (Fig. 3*J*). However, it cannot be excluded that the separation may in part be caused by a systematic variance introduced between the two measurements. Applied to a dataset acquired from cocultured cells using the same coordinate system, the PCA produced two clusters similar to those detected for monocultures, with less separation (Fig. 3*J*). Coloring each cell according to the classification based on ML confirms that the clusters representing each cell type are less distinct and partly overlap (Fig. 3*K*). This effect may be explained by changes in the molecular profile of both cell types in response to exposure to each other, or even as the result of a molecular exchange between the two cell types.

The combination of the two approaches, SVM and PCA, provides for a clear separation and visualization of the results. While the SVM utilizes the rich 500-dimensional information of the mass spectra to classify all cells with high accuracy when using an appropriate training set, the visualization in a PCA plot intuitively allows selecting single cells based on separation characteristics (or, in other words, their position in the PCA score plot). This feature can be used to individually study and compare histological phenotypes with individual mass spectra of selected cells that are assigned as distinctly different by the PCA. Highlighted in Fig. 3*K* as two examples, Fig. 3*L* and *M* provide the optical images for two cells, color-coded in blue (Caki-2) and red (Vero-B4), respectively. Fig. 3*N* displays differences in their mass spectra. As this process is of a bidirectional nature, a group of specific cells could also be selected based on histological information (e.g., distance to cells of the other cell type) and a resulting point cloud within the score plot of the PCA could be examined for clustering. Additionally, mass spectra could be extracted for these potential clusters and analyzed with regard to molecular markers of the selected histological phenotype.

In case no monocultures of cells are available, training sets can be compiled manually based on histological features or distinct *m/z* channels and applied to a much larger cohort of cells within the same measurement.

Intercellular Heterogeneity. Next, we used the developed workflow to characterize molecular heterogeneity in the same datasets as analyzed above. Here, the cocultivation of Vero-B4 and Caki-2 served as a model system for a heterogeneous cell population. MALDI-2-MSI data collected in positive-ion mode from the sample system produced information-rich spectra. Based on a comparison with comprehensive high-performance liquid chromatography electrospray ionization ion mobility tandem mass spectrometry (HPLC-ESI-IMS-MS/MS) lipidomics analysis of cell extracts and linked by exact molecular mass and isotopic pattern quality, a total of 99 different lipid species from 8 lipid classes were tentatively assigned in the MALDI-2-MSI data (cf *SI Appendix, Methods* and *Table S3* for details on ESI-based lipidomics and lipid assignments). In addition, for selected lipid ion species, annotation was confirmed using

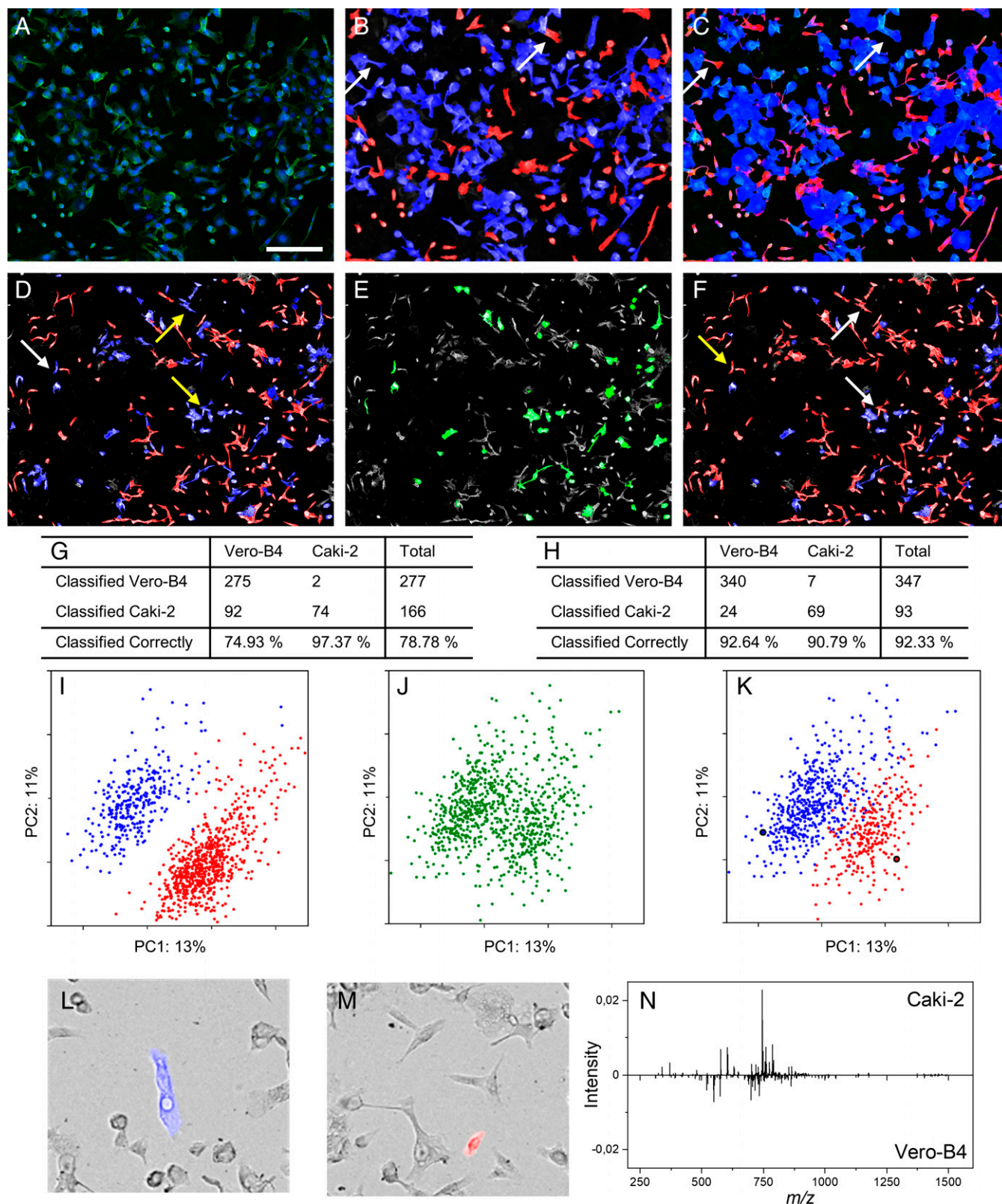


Fig. 3. Classification results for cocultured Vero-B4 and Caki-2 cells. (A) Microscopy overlay of the WGA and DAPI channels. (B) Classification results for the cocultured system using an SVM based on single-cell mass spectra, trained with a set of a few hundred m/z values on the respective monocultures. (C) Classification of the coculture based on three microscopic images (bright-field, Hoechst stain, and WGA stain) using Olympus TruAI software, trained on the respective monocultures. White arrows point to differences in the classification for individual cells. (D) Classification results for a biological replicate of the cocultured system using the SVM trained on the original dataset. (E) Ground-truth identification of Vero-B4 (gray) and Caki-2 cells (green) based on live-cell staining. (F) Classification results for the biological replicate of the cocultured system using the SVM trained on a dataset based on the same cell cultures. Arrows are used to point to exemplary differences in classification in D and F: white arrows, cells correctly classified; yellow arrows, cells misclassified according to the ground-truth data. (G and H) Numerical classification results of D (trained on a different biological replicate) and F (trained on the same biological replicate). (I–K) Unsupervised statistical analysis: PCA of pooled data from (I) both monocultures, (J) the coculture, and (K) the coculture, with cells colored according to their classification by the SVM. (L–M) Microscopy images of individual Caki-2 (L; colored in blue) and Vero-B4 (M; colored in red) cells, as selected and marked in the PCA plot with outlines, and (N) their respective MALDI-2 difference mass spectra. (Scale bar, 200 μm .)

MALDI-2-MS/MS analysis directly from cell culture (*SI Appendix, Figs. S8–S20*).

For analysis of heterogeneity, data collected from monocultures of each cell line are compared using univariate statistics. This allowed us to identify molecular species with the highest fold change (FC) between the two cultures (see *SI Appendix, Fig. S6* for a volcano plot representation) that may carry useful information on the origin and function of the specific cell types (see *SI Appendix, Fig. S7* for images). Signal intensities at m/z values of 630.619 and 632.624 with an FC of 2.9 and 3.6 have been assigned to $[\text{Cer}(\text{d18:1/24:1})-\text{H}_2\text{O}+\text{H}]^+$ and $[\text{Cer}(\text{d18:1/24:0})-\text{H}_2\text{O}+\text{H}]^+$ ceramides, respectively. Signals at m/z 862.620 and 700.575 represent $[\text{Hex2Cer}(\text{d18:1/16:0})+\text{H}]^+$ and $[\text{HexCer}(\text{d18:1/16:0})+\text{H}]^+$ hexosylceramides and display a respective FC of 0.42 and 0.40. While a detailed analysis of cell biological implications is beyond the scope of this study, the observed elevated concentrations of ceramide species found in Caki-2 cells can be attributed to the cell line's origin in cancer. Cancerous cells have been reported to express elevated levels of ceramides (51). Vero-B4 cells, on the other hand, are derived from healthy tissue and have been described to be rich in glycosphingolipids such as monohexosyl- and lactosylceramides as part of their cell-to-cell signaling system (52).

Molecular heterogeneity within the full cell population, but also within each individual group of cells, can be displayed in the form of histograms (Fig. 4). Histograms can visualize signal intensity distributions within a group of cells by sorting them into bins according to the intensity of the corresponding ion signal in their single-cell mass spectra. As a result, the histogram displays the number of cells in each intensity bin in the form of a bar chart. A single narrow Gaussian-type histogram describes similar signal intensities generated for every cell. In our model system, this type of distribution is, for example, found for $[\text{DAG}(34:1)-\text{H}_2\text{O}+\text{H}]^+$ at m/z 577.520 (Fig. 4*A*) in all investigated cell cultures. As described above, this lipid ion species most likely originates from fragmentation of several precursors of different lipid classes with the same composition of acyl chains. Broader peaks with wide distribution, on the other hand, are indicative of heterogeneity within the cell population, for example $[\text{HexCer}(\text{d18:1/16:0})+\text{H}]^+$ in Vero-B4 cells (Fig. 4*B*) and $[\text{Cer}(\text{d18:1/24:1})-\text{H}_2\text{O}+\text{H}]^+$ in Caki-2 cells (Fig. 4*C*). The occurrence of more than one signal intensity distribution, separated in the histogram, points to distinctly different populations within the cell culture. In our model system, these two populations are simulated by mixing two similar but different cell lines. For the coculture, the respective histogram for $[\text{HexCer}(\text{d18:1/16:0})+\text{H}]^+$ presents a partly resolved bimodal distribution that can be interpreted as an overlay of the histograms produced by the respective monocultures. However, in most cases, these distributions show a substantial overlap and do not allow for a clear separation based on a single histogram alone.

For a clearer interpretation, individual signal intensity distributions can also be compiled for the different groups of cells identified by classification. This enables the investigation of homo- and heterogeneity within each individual class of cells within the coculture and the contribution of each individual cell class to the overall sum histogram. Applied to our model system, signal intensity distributions of $[\text{HexCer}(\text{d18:1/16:0})+\text{H}]^+$ for the two monocultured cell types reveal obvious differences. As expected from the visible overlap of these two distributions, however, no clear bimodality is discernable in the coculture. After sorting cells based on their classification, histograms for both groups of cells can be produced for this molecular ion species, reproducing two distinctly different distributions similar to those observed in the respective

monocultures. Interestingly, the presented signal intensity distributions of $[\text{Cer}(\text{d18:1/24:1})-\text{H}_2\text{O}+\text{H}]^+$ reveal a change in expression and heterogeneity between mono- and coculture. The ceramide signal intensity sizably increases for Vero-B4 cells when cocultured together with Caki-2 cells. Again, a clear separation of distributions in the histogram is facilitated by the use of information from prior classification. In line with the literature, the observed changes in ceramide signal intensity in Vero-B4 cells could point to stress that is induced by the coculturing with Caki-2 cells (51). In this context, it may be speculated that tumor necrosis factor alpha, described to be up-regulated in Caki-2 cells, is secreted, and induces the production of ceramides in the cocultured Vero-B4 cells (53, 54).

Cellular Heterogeneity during Differentiation. In a second example, we used THP-1 cells to investigate molecular changes during differentiation from monocytes to macrophages by the addition of phorbol 12-myristate 13-acetate (PMA) (55) (see *SI Appendix, Methods and Fig. S21* for more information). Cells were harvested 24, 48, and 72 h after differentiation was induced and analyzed using the workflow presented above. PCA of the resulting single-cell mass spectra reveals distinguishable molecular profiles between populations 24 h (monocyte) and 72 h (macrophage) after stimulation (Fig. 5*A*) with little overlap. After 48 h, most cells express a transiting molecular profile somewhat “in-between” monocyte and macrophage. During this transit stage, some cells, however, still express the molecular profile of monocytes, while others are found to already fully resemble the lipid profile of macrophages. In contrast to a bulk analysis, this heterogeneity in differentiation between individual cells is only accessible using single-cell data. To reveal lipid ion species that discriminate between the stages of differentiation within the cell culture, we used a volcano plot (*SI Appendix, Fig. S22*). Fig. 5 displays intensity histograms for a triacylglycerol $[\text{TAG}(50:1)+\text{H}]^+$ at m/z 833.653 (Fig. 5*B*), $[\text{PE}(38:2)+\text{H}]^+$ at m/z 772.583 (Fig. 5*C*), and $[\text{PE}(38:5)+\text{H}]^+$ at m/z 766.538 (Fig. 5*D*) (annotations are based on MS/MS; *SI Appendix, Figs. S18–S20*). These histograms reveal a gradual increase for TAG(50:1) and a gradual decrease for PE(38:2) in the investigated cells over 72 h after stimulation. TAG(50:1) signal intensities show a narrow and unimodal signal distribution at low intensity values for the monocytes and stronger heterogeneity visualized by a broad, possibly multimodal, distribution at a higher level of lipid expression, presumably representing different stages of macrophage differentiation. While a detailed biological analysis of these findings was beyond the scope of this study, increasing levels of TAGs could point to an activation of THP-1 cells via the proinflammatory pathway as described in the literature (56, 57). For PE(38:2), this trend is reversed, revealing a high and broadly distributed expression in monocytes and decreased and narrowly distributed signal intensity after differentiation. No change in lipid expression during differentiation was observed for PE(38:5). The “molecular phenotypes” identified by specific lipid expression can be compared with microscopic images of representative cells. Typical examples are presented as insets in Fig. 5. The selected cell with a high signal intensity for PE(38:2) and a low expression of TAG is spherical with a smooth surface typical for monocytes. A characteristic cell with high levels of TAG and decreased expression of PE(38:2) is larger and displays a more spread-out morphology with folds and thin protrusions visible on the surface, typical for macrophages. As expected from the data, both selected cells show similar signal intensities for PE(38:5).

Intracellular Heterogeneity. Fig. 6 displays ion intensity distributions for a number of lipid species recorded at a pixel size of 2 μm .

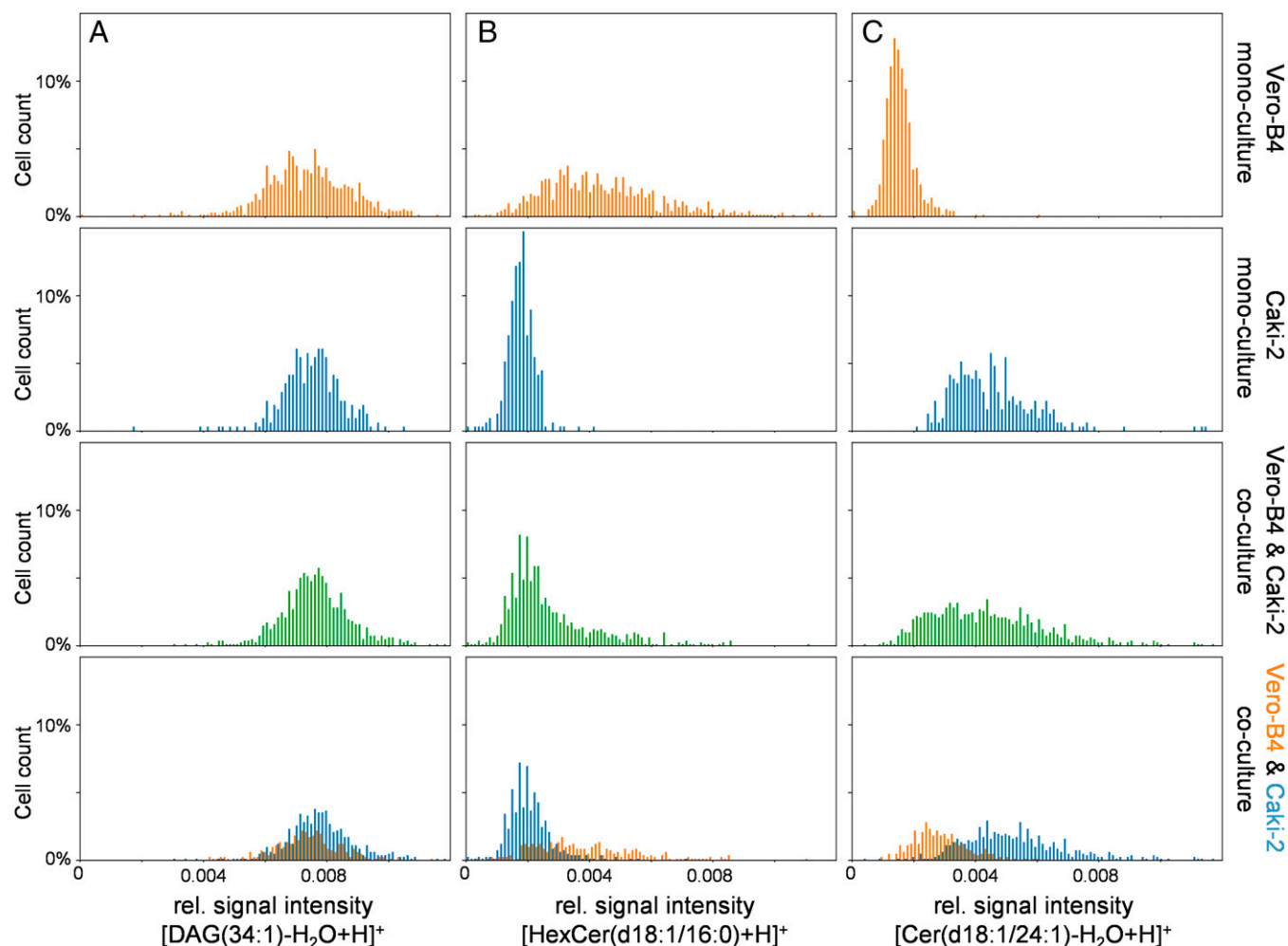


Fig. 4. Histograms of selected ion signal intensities for mono- and cocultured Vero-B4 and Caki-2 cells. (A) Histograms for $[\text{DAG}(34:1)\text{-H}_2\text{O}+\text{H}]^+$ found with a homogeneous distribution in both cell types with similar ion intensities. (B) Histograms for $[\text{HexCer}(d18:1/16:0)+\text{H}]^+$ with a homogeneous distribution in Caki-2 and heterogeneous distribution in Vero-B4 monocultures and a broad, overlapping distribution in coculture. (C) Histograms for $[\text{Cer}(d18:1/24:1)\text{-H}_2\text{O}+\text{H}]^+$ displaying a heterogeneous distribution in Caki-2 and homogeneous distribution in Vero-B4 monocultures but a heterogeneous distribution for both cell types in coculture. (Bottom) Overlay of histograms of subpopulations within the coculture based on classification results described in the text.

While 8- μm pixels enable the investigation of intercellular heterogeneity, this reduced pixel size permits a glimpse at the molecular distributions within individual cells. While some signals are distributed evenly throughout the whole

cell culture (Fig. 6A), for others more regional differences inside individual cells can be observed. This may include a predominant localization close to the cell nucleus or in the periphery of the cell membrane (Fig. 6B) or in discrete

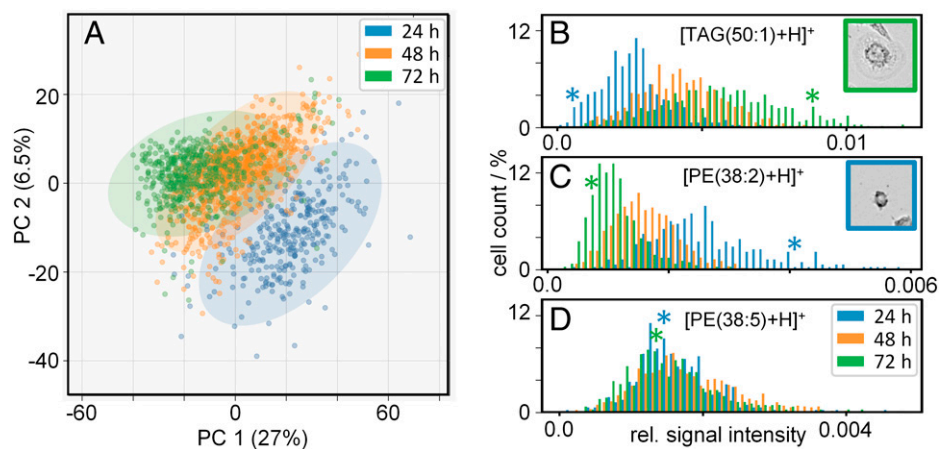


Fig. 5. (A) PCA based on single-cell mass spectra of THP-1 cells for three time points during differentiation from monocytes to M0 macrophages. (B–D) Histograms of selected ion signal intensities. Cells show (B) an increase of $[\text{TAG}(50:1)+\text{H}]^+$ signal and (C) a decrease of $[\text{PE}(38:2)+\text{H}]^+$ signal during differentiation. (D) For $[\text{PE}(38:5)+\text{H}]^+$, no change is observed. Differences in lipid expression profiles correlate with changes in morphology from typical monocyte cells at 24 h (e.g., cell in blue square) to typical macrophage cells at 72 h (green square). Asterisks indicate the position of the selected cells in the histograms.

clusters randomly distributed in the cell body (Fig. 6D). Other lipid ion species show strong differences between individual cells as described above (Fig. 6C). Besides opening the door to subcellular molecular imaging using t-MALDI-2-MSI, these results demonstrate the importance of a complete sampling of cell material in single-cell analysis. Sizable undersampling of the cell may result in the random under- or overrepresentation of molecular ion species with different subcellular distribution in the resulting single-cell mass spectra that can artificially broaden the resulting signal intensity distributions.

Extending this qualitative analysis, we studied the complex interrelations between intracellular and intercellular heterogeneity by comparing intensity distributions on the single-cell level with the single-pixel level. For this, the described workflow was expanded by treating all pixels that are located on a cell individually to produce additional signal intensity distributions on the pixel level. Applied to data acquired from Vero-B4 cells using t-MALDI-2-MSI at a 2- μm pixel size, a total of 98 cells are identified with 29,096 pixels connected to these cells. To visualize the pairwise correlation between selected biologically interesting phospho- and glycosphingolipids on a pixel as well as single-cell level, we plotted the signal intensities in correlation plots. Displayed in Fig. 6, every data point in these plots represents one cell or pixel, respectively, and signal intensities for the two lipid ion species are plotted on the respective axis. By comparing the signal intensity of two different lipid ion species at

specific positions within the cells, it is possible to draw conclusions on regional correlation at the spatial resolution dictated by pixel size. While two lipid species may show a strong correlation on the level of the whole cell, they may be expressed in different parts of the cell, reflected in a low correlation on the level of single pixels. On the level of complete cells, high intracellular heterogeneity has no impact on the correlation, while a strong intercellular variation results in a low correlation index. A visible difference in the correlation between the level of complete cells and individual pixels therefore indicates intracellular heterogeneity.

For $[\text{PE}(34:1)+\text{H}]^+$ and $[\text{PE}(36:2)+\text{H}]^+$, single-cell data as well as individual pixels show a high Pearson correlation coefficient (PCC) (Fig. 6A). Expression of these two lipid species is highly correlated not only on the level of the complete cell but also with regard to their distribution within the cellular body. Comparing the abundant ion signal intensities of $[\text{PE}(36:2)+\text{H}]^+$ and $[\text{PC}(34:1)+\text{H}]^+$ reveals a similarly high correlation on the cellular level with a PCC of 0.95 (Fig. 6B) yet a slightly different spatial distribution within the individual cell is reflected in a decreased PCC on the pixel level. As visualized in the MS images, $[\text{PC}(34:1)+\text{H}]^+$ is preferably detected from the inner cell and near the nucleus, while $[\text{PE}(36:2)+\text{H}]^+$ is also detected near the edges of the cell. Stronger effects of the same sort are observed for the pairwise correlation of $[\text{HexCer}(\text{d}18:1/16:0)+\text{H}]^+$ and $[\text{Cer}(\text{d}18:1/16:0)+\text{H}]^+$ displayed in Fig. 6C. While a PCC of 0.88 indicates a loose correlation on the cellular level, much lower

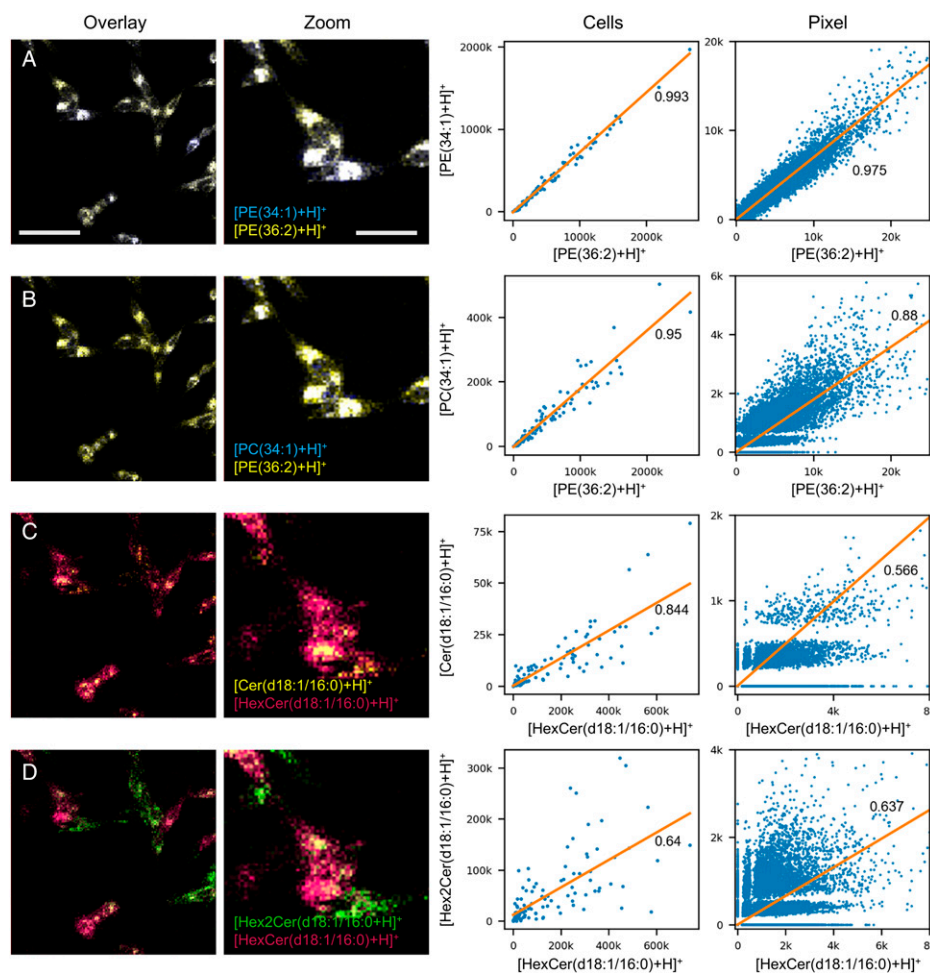


Fig. 6. Visualization of inter- and intracellular heterogeneity for Vero-B4 cells of selected ions. (Left) t-MALDI-2-MS images of the respective m/z values at a pixel size of 2 μm and a zoom-in of individual cells point to different characteristics of heterogeneity. (Right) Correlation plots for selected lipid ion pairs on the single-cell and cell-associated pixel level. (A) $[\text{PE}(34:1)+\text{H}]^+$ and $[\text{PE}(36:2)+\text{H}]^+$. (B) $[\text{PC}(34:1)+\text{H}]^+$ and $[\text{PE}(36:2)+\text{H}]^+$. (C) $[\text{HexCer}(\text{d}18:1/16:0)+\text{H}]^+$ and $[\text{Cer}(\text{d}18:1/16:0)+\text{H}]^+$. (D) $[\text{HexCer}(\text{d}18:1/16:0)+\text{H}]^+$ and $[\text{Hex2Cer}(\text{d}18:1/16:0)+\text{H}]^+$. (Scale bars, 100 and 50 μm [zoom-in].)

correlation is found in the pixel domain. Particularly pronounced for the ceramide depicted on the ordinate of the correlation plot, signal intensity distributions on the pixel level split up into distinctly separated groups. This indicates specific areas of high and low levels of the investigated lipids within the cell. These areas are also found in the respective MS images in the form of subcellular domains, typically >4 to 6 μm in diameter. Corroborating these results, ceramides have been described to form domains within the cellular membrane of similar size (58). A different picture is found for the pairwise correlation of the glycosphingolipids [HexCer(d18:1/16:0)+H]⁺ and [Hex2Cer(d18:1/16:0)+H]⁺. In this example, strong heterogeneity is visible already on the intercellular level. Consequently, the PCC for the complete cell population as well as individual pixels is low. Again, these findings are corroborated by previous reports based on single-cell MSI describing a strong cell-to-cell variability in the expression of glycosphingolipids (16).

Conclusion

The combination of light microscopy and MALDI-MS imaging of cultured cells at a pixel size below 10 μm enabled lipid MS analysis on the single-cell level. In contrast to techniques that rely on isolation and/or pooling of single cells, the presented approach minimizes perturbation of cells prior to analysis and produces single-cell mass spectra directly interconnected with microscopy-based histological information for each individual cell in its original surrounding. The application of streamlined fixation and matrix preparation protocols as well as the use of chamber slides minimized sample preparation time. The use of state-of-the-art MS technology reduced time of analysis of hundreds of individual cells to under an hour. While techniques employing a larger pixel size may be even faster, our approach includes 90% of all cell-related pixels with their full pixel area omitting ambiguities in mass spectra introduced by undersampling parts of the investigated cells.

Key elements of the presented workflow included segmentation and coregistration of the two imaging modalities and subsequent assignment of each MS pixel to a specific individual cell or to the background. These steps were facilitated by staining protocols compatible with MALDI-MSI analysis and optical analysis prior to matrix application. While for cell cultures that were grown to subconfluence, as presented in this work, simple and robust segmentation algorithms are sufficient for segmentation and classification, more sophisticated tools may be required in the analysis of complex multicellular samples like organoids or full tissue sections (35, 50). Here, the use of alternative MALDI-compatible staining methods may also be of help.

Unambiguous assignment of pixels to specific cells allows the compilation of datasets consisting of single-cell mass spectra that can be analyzed and classified using ML as well as multi- and univariate statistics based on their molecular profile. Using the direct connection between the employed modalities allows evaluating the resulting groups of molecularly similar cells regarding optical features such as morphology, phenotype, and cellular “neighborhood.” Signal intensity histograms based on single-cell mass spectra are especially useful to investigate intercellular heterogeneity within the complete cell culture or to identify subpopulations. In the future, such identified subpopulations with specific changes in the lipidome may act as an important initial starting point to investigate changes and differences in the up- and downstream metabolic pathways using complementary techniques such as immunohistochemistry, single-cell messenger RNA sequencing, or targeted protein analysis.

Furthermore, the use of t-MALDI-2-MS imaging employing a pixel size of $\leq 2 \mu\text{m}$ enables the investigation of intracellular heterogeneity on a molecular level. Analysis of molecular information on the micrometer-sized pixel level allowed to identifying subcellular structures common to a large number of cells. In this regard, our results may be viewed as a promising step toward developing a true subcellular analysis using MALDI-MSI.

Materials and Methods

Chemicals. All chemicals and organic solvents were from Merck (Sigma-Aldrich) unless otherwise noted.

Cell Culture. Cells were cultivated and cultures were prepared for the subsequent microscopic and MALDI-MSI analyses as described before (44). Modifications in terms of a staining step have been added to the standard protocol. For a detailed description, please refer to *SI Appendix*.

For cocultivation experiments, Caki-2 and Vero-B4 cells were grown as mono- as well as cocultures in different chambers of the same slide. Two biological replicates were generated with one containing Caki-2 cells stained with a live-cell dye (CellTracker Deep Red, Fisher Chemical, 5 μM , 45 min) prior to cocultivation to enable the assignment of the correct cell type in the coculture experiment.

THP-1 cells were differentiated to macrophages by stimulation of the monocytes with 200 ng/mL PMA for 24, 48, and 72 h.

Microscopy. Bright-field and fluorescent microscopic images were acquired with a digital slide scanner (SLIDEVIEW VS200, Olympus). For details, please refer to *SI Appendix*.

MALDI-2-MSI. The mass spectrometer and respective methods for the analysis of single cells employed for t-MALDI-2-MSI at a 2- μm pixel size have been described in detail previously (39, 44). The mass spectrometer used for top illumination was a timsTOF fleX with MALDI-2 (Bruker Daltonics) described elsewhere (42). For a more detailed description, please refer to *SI Appendix*.

Data Processing. For both Orbitrap and timsTOF measurements, SCiLS Lab MVS software (v. 2021a Pro, SCiLS Lab/Bruker Daltonics) was used to generate ion images with a reduced-mass list of the most prominent peaks in the csv or imzML format (59) for further processing in Python. For a more detailed description, please refer to *SI Appendix*.

Single-Cell Segmentation. For single-cell segmentation, local maxima in the fluorescence microscopy DAPI channel were declared as cell seeds and a watershed algorithm (skimage 0.14.0) attributed each pixel to either a certain seed or background based on the fluorescence microscopy fluorescein isothiocyanate (FITC) channel. For a more detailed description, please refer to *SI Appendix*.

Coregistration of MALDI-MSI and Microscopy Data and Compilation of Single-Cell Mass Spectra. For the coregistration, a correlation of binarized MALDI and binarized microscopy images was used. The MALDI-MSI data were imported to Python with pyimzML 1.3.0 or directly via csv files (60) and binarized using a threshold signal intensity of an m/z value that is omnipresent in the cells but absent in the background. The binarized MALDI images were then resized to an artificial pixel size of 1 μm (e.g., a pixel with $2 \times 2 \mu\text{m}$ would be transformed into four $1 \times 1 \mu\text{m}$ pixels with the same values). Likewise, the microscopy images were binarized to cell area and background based on the FITC channel, and resized to a pixel size of 1 μm as well. Pixels in both binarized images were set to a value of 1 for MALDI signal/cell area and -1 for background. The binary MALDI images were used as the kernel for a two-dimensional correlation (1- μm step size) with the binary microscopy images (using `scipy.signal.correlate2d`). MALDI signal pixels matching cell-area pixels contributed positively as well as background pixels matching background pixels. Conversely, matches of MALDI signal pixels with background pixels and cell-area pixels with background pixels contributed negatively to the correlation value. The position with the maximum correlation was used for a preliminary coregistration. Around this position, all combinations of a set of rotations (0.1° step size between -2.5 and 2.5°) and positions (1- μm step size in a $50 \times 50 \mu\text{m}$ rectangle) were tested in a brute-force approach and the combination of rotation and

position for which the correlation of binarized MALDI and microscopy images was maximal was used for coregistration.

After the coregistration, the original MALDI images (original pixel size and nonbinarized) were used to retrieve the MALDI-based MS information for each individual cell. MALDI pixels that touched two cells were discarded. Pixels that contained only one cell but also background were treated as if the measured intensities stemmed just from the cell. Finally, all pixels overlapping with a single cell were summed up to retrieve a MALDI spectrum for that specific individual cell.

Cell Classification Ground Truth Based on Live-Cell Dye. Selective live-cell staining of Caki-2 cells allowed the collection of a ground truth for the cocultivated cell cultures based on the average fluorescence intensity per area of each cell in the fluorescence microscopy Cy5 channel. For a more detailed description, please refer to *SI Appendix*.

Statistical Analysis and SVM Classification. Single-cell mass spectra were normalized to the TIC. Monocultivated cells were used as labeled training data and randomly partitioned into five equal-sized subsamples for fivefold cross-validation. The Python package scikit-learn 0.21.3 was used to create a pipeline of mean centering, scaling to unit variance and a linear SVM with balanced class weightings. After confirming precise classification accuracies, the pipeline was retrained on all monocultivated cells and then used to classify the cocultivated cells. For a description of other statistical tools, please refer to *SI Appendix*.

Data Availability. All study data and meta information as well as original code are available from the authors upon request. Raw data for MALDI-MSI and

lipidomics studies are available as a vendor neutral imzML and/or proprietary file format. In addition, some of the MALDI imaging data reported in this article have been uploaded to the METASPACE annotation platform to be viewed directly by the interested reader (https://metaspace2020.eu/project/bien_cellular_heterogeneity?tab=datasets) (61).

ACKNOWLEDGMENTS. We thank Dagmar Mense and Nicola Skutta for expert help with cell cultivation, Johannes Muthing for helpful discussions, Stephanie Reisewitz and Alexander Müller-Nedebock from Olympus Deutschland GmbH for providing the VS200 digital slide scanner, Eric Stellamanns (Olympus) for instrument assistance, Bruker Daltonics for instrument assistance and support of the project, and Ansgar Korf and Viola Jeck (both from Bruker) for help with ESI-based lipidomics analysis. Financial support by the German Research Foundation (DFG; Grants DR416/12-1 and SO976/3-1, Project No. 290343045 [to K.D. and J. Soltwisch] and Grant SO976/5-1, Project No. 400912714 [to J. Soltwisch]), the Interdisciplinary Center for Clinical Research (IZKF) of the University of Münster Medical School (Grant Drei2/018/17 [to K.D. and J. Soltwisch]), and the fund Innovative Medical Research of the University of Münster Medical School (Grant SO 12 19 11) to J. Soltwisch is gratefully acknowledged.

Author affiliations: ^aInstitute of Hygiene, University of Münster, 48149 Münster, Germany; ^bInterdisciplinary Center for Clinical Research (IZKF), University of Münster, 48149 Münster, Germany; ^cInstitute for Psychology, University of Münster, 48149 Münster, Germany; and ^dOtto Creutzfeldt Center for Cognitive and Behavioural Neuroscience, University of Münster, 48149 Münster, Germany

1. L. Armbricht, P. S. Dittrich, Recent advances in the analysis of single cells. *Anal. Chem.* **89**, 2–21 (2017).
2. M. J. Taylor, J. K. Lukowski, C. R. Anderton, Spatially resolved mass spectrometry at the single cell: Recent innovations in proteomics and metabolomics. *J. Am. Soc. Mass Spectrom.* **32**, 872–894 (2021).
3. S. V. Avery, Microbial cell individuality and the underlying sources of heterogeneity. *Nat. Rev. Microbiol.* **4**, 577–587 (2006).
4. C. J. Davidson, M. G. Surette, Individuality in bacteria. *Annu. Rev. Genet.* **42**, 253–268 (2008).
5. A. Raj, A. van Oudenaarden, Nature, nurture, or chance: Stochastic gene expression and its consequences. *Cell* **135**, 216–226 (2008).
6. S. J. Altschuler, L. F. Wu, Cellular heterogeneity: Do differences make a difference? *Cell* **141**, 559–563 (2010).
7. B. Yang, N. H. Patterson, T. Tsui, R. M. Caprioli, J. L. Norris, Single-cell mass spectrometry reveals changes in lipid and metabolite expression in RAW 264.7 cells upon lipopolysaccharide stimulation. *J. Am. Soc. Mass Spectrom.* **29**, 1012–1020 (2018).
8. D. Cohen *et al.*, Chemical cytometry: Fluorescence-based single-cell analysis. *Annu. Rev. Anal. Chem. (Palo Alto, Calif.)* **1**, 165–190 (2008).
9. A. Amantonic, P. L. Urban, R. Zenobi, Analytical techniques for single-cell metabolomics: State of the art and trends. *Anal. Bioanal. Chem.* **398**, 2493–2504 (2010).
10. B. Hwang, J. H. Lee, D. Bang, Single-cell RNA sequencing technologies and bioinformatics pipelines. *Exp. Mol. Med.* **50**, 1–14 (2018).
11. E. Z. Macosko *et al.*, Highly parallel genome-wide expression profiling of individual cells using nanoliter droplets. *Cell* **161**, 1202–1214 (2015).
12. A.-D. Brunner *et al.*, Ultra-high sensitivity mass spectrometry quantifies single-cell proteome changes upon perturbation. *Mol. Syst. Biol.* **18**, e10798 (2022).
13. A. Amantonic, J. Y. Oh, J. Sobek, M. Heinemann, R. Zenobi, Mass spectrometric method for analyzing metabolites in yeast with single cell sensitivity. *Angew. Chem. Int. Ed. Engl.* **47**, 5382–5385 (2008).
14. E. K. Neumann, T. J. Comi, S. S. Rubakhin, J. V. Sweedler, Lipid heterogeneity between astrocytes and neurons revealed by single-cell MALDI-MS combined with immunocytochemical classification. *Angew. Chem. Int. Ed. Engl.* **58**, 5910–5914 (2019).
15. Z. Li *et al.*, Single-cell lipidomics with high structural specificity by mass spectrometry. *Nat. Commun.* **12**, 2869 (2021).
16. L. Capolupo *et al.*, Sphingolipid control of fibroblast heterogeneity revealed by single-cell lipidomics. <https://doi.org/10.1126/science.abh1623> (Accessed 3 April 2022).
17. B. Snijder *et al.*, Population context determines cell-to-cell variability in endocytosis and virus infection. *Nature* **461**, 520–523 (2009).
18. M. Denz *et al.*, Cell cycle dependent changes in the plasma membrane organization of mammalian cells. *Biochim. Biophys. Acta Biomembr.* **1859**, 350–359 (2017).
19. L. Zhang, A. Vertes, Single-cell mass spectrometry approaches to explore cellular heterogeneity. *Angew. Chem. Int. Ed. Engl.* **57**, 4466–4477 (2018).
20. L. Yin, Z. Zhang, Y. Liu, Y. Gao, J. Gu, Recent advances in single-cell analysis by mass spectrometry. *Analyst (Lond.)* **144**, 824–845 (2019).
21. H.-M. Bergman, K. D. Duncan, I. Lanekoff, "Single-cell mass spectrometry" in *Encyclopedia of Analytical Chemistry*. R. A. Meyers, Ed. (John Wiley & Sons, 2018), pp. 1–19.
22. M. K. Passarelli, A. G. Ewing, Single-cell imaging mass spectrometry. *Curr. Opin. Chem. Biol.* **17**, 854–859 (2013).
23. A. Amantonic, P. L. Urban, S. R. Fagerer, R. M. Balabin, R. Zenobi, Single-cell MALDI-MS as an analytical tool for studying intrapopulation metabolic heterogeneity of unicellular organisms. *Anal. Chem.* **82**, 7394–7400 (2010).
24. P. V. Shanta, B. Li, D. D. Stuart, Q. Cheng, Plasmonic gold templates enhancing single cell lipidomic analysis of microorganisms. *Anal. Chem.* **92**, 6213–6217 (2020).
25. P. L. Urban *et al.*, High-density micro-arrays for mass spectrometry. *Lab Chip* **10**, 3206–3209 (2010).
26. A. J. Ibáñez *et al.*, Mass spectrometry-based metabolomics of single yeast cells. *Proc. Natl. Acad. Sci. U.S.A.* **110**, 8790–8794 (2013).
27. J. Krismer *et al.*, Screening of *Chlamydomonas reinhardtii* populations with single-cell resolution by using a high-throughput microscale sample preparation for matrix-assisted laser desorption/ionization mass spectrometry. *Appl. Environ. Microbiol.* **81**, 5546–5551 (2015).
28. J. Krismer, M. Tamminen, S. Fontana, R. Zenobi, A. Narwani, Single-cell mass spectrometry reveals the importance of genetic diversity and plasticity for phenotypic variation in nitrogen-limited *Chlamydomonas*. *ISME J.* **11**, 988–998 (2017).
29. T. H. Ong *et al.*, Classification of large cellular populations and discovery of rare cells using single cell matrix-assisted laser desorption/ionization time-of-flight mass spectrometry. *Anal. Chem.* **87**, 7036–7042 (2015).
30. E. T. Jansson, T. J. Comi, S. S. Rubakhin, J. V. Sweedler, Single cell peptide heterogeneity of rat islets of Langerhans. *ACS Chem. Biol.* **11**, 2588–2595 (2016).
31. T. J. Comi, E. K. Neumann, T. D. Do, J. V. Sweedler, microMS: A Python platform for image-guided mass spectrometry profiling. *J. Am. Soc. Mass Spectrom.* **28**, 1919–1928 (2017).
32. T. J. Comi, T. D. Do, S. S. Rubakhin, J. V. Sweedler, Categorizing cells on the basis of their chemical profiles: Progress in single-cell mass spectrometry. *J. Am. Chem. Soc.* **139**, 3920–3929 (2017).
33. W. Xie, D. Gao, F. Jin, Y. Jiang, H. Liu, Study of phospholipids in single cells using an integrated microfluidic device combined with matrix-assisted laser desorption/ionization mass spectrometry. *Anal. Chem.* **87**, 7052–7059 (2015).
34. L. Rappez *et al.*, SpaceM reveals metabolic states of single cells. *Nat. Methods* **18**, 799–805 (2021).
35. K. Ščupáková, F. Dewez, A. K. Walch, R. M. A. Heeren, B. Balluff, Morphometric cell classification for MALDI-mass spectrometry imaging. *Angew. Chem. Int. Ed. Engl.* **59**, 17447–17450 (2020).
36. T. Bien *et al.*, MALDI-2 mass spectrometry and immunohistochemistry imaging of Gb3Cer, Gb4Cer, and further glycosphingolipids in human colorectal cancer tissue. *Anal. Chem.* **92**, 7096–7105 (2020).
37. M. Kompauer, S. Heiles, B. Spengler, Atmospheric pressure MALDI mass spectrometry imaging of tissues and cells at 1.4-μm lateral resolution. *Nat. Methods* **14**, 90–96 (2017).
38. A. Zavalin *et al.*, Direct imaging of single cells and tissue at sub-cellular spatial resolution using transmission geometry MALDI MS. *J. Mass Spectrom.* **47**, 1473–1481 (2012).
39. M. Niehaus, J. Soltwisch, M. E. Belov, K. Dreisewerd, Transmission-mode MALDI-2 mass spectrometry imaging of cells and tissues at subcellular resolution. *Nat. Methods* **16**, 925–931 (2019).
40. J. Soltwisch *et al.*, Mass spectrometry imaging with laser-induced postionization. *Science* **348**, 211–215 (2015).
41. S. R. Ellis, J. Soltwisch, M. R. L. Paine, K. Dreisewerd, R. M. A. Heeren, Laser post-ionisation combined with a high resolving power Orbitrap mass spectrometer for enhanced MALDI-MS imaging of lipids. *Chem. Commun. (Camb.)* **53**, 7246–7249 (2017).
42. J. Soltwisch *et al.*, MALDI-2 on a trapped ion mobility quadrupole time-of-flight instrument for rapid mass spectrometry imaging and ion mobility separation of complex lipid profiles. *Anal. Chem.* **92**, 8697–8703 (2020).
43. M. S. Boskamp, J. Soltwisch, Charge distribution between different classes of glycerophospholipids in MALDI-MS imaging. *Anal. Chem.* **92**, 5222–5230 (2020).
44. T. Bien, S. Bessler, K. Dreisewerd, J. Soltwisch, Transmission-mode MALDI mass spectrometry imaging of single cells: Optimizing sample preparation protocols. *Anal. Chem.* **93**, 4513–4520 (2021).
45. N. H. Patterson, E. Yang, E.-A. Kranjec, P. Chaurand, Co-registration and analysis of multiple imaging mass spectrometry datasets targeting different analytes. *Bioinformatics* **35**, 1261–1262 (2019).
46. K. A. Veselkov *et al.*, Chemo-informatic strategy for imaging mass spectrometry-based hyperspectral profiling of lipid signatures in colorectal cancer. *Proc. Natl. Acad. Sci. U.S.A.* **111**, 1216–1221 (2014).
47. W. M. Abdelmoula *et al.*, Automatic generic registration of mass spectrometry imaging data to histology using nonlinear stochastic embedding. *Anal. Chem.* **86**, 9204–9211 (2014).

48. A. Nikitina *et al.*, A co-registration pipeline for multimodal MALDI and confocal imaging analysis of stem cell colonies. *J. Am. Soc. Mass Spectrom.* **31**, 986–989 (2020).
49. S. Nam *et al.*, Introduction to digital pathology and computer-aided pathology. *J. Pathol. Transl. Med.* **54**, 125–134 (2020).
50. M. Genenger, M. Woerdemann, TruAI Based on Deep-Learning Technology for Robust, Label-Free Nucleus Detection and Segmentation in Microwell Plates (2021). https://www.olympus-lifescience.com/de/resources/white-papers/label-free_segmentation (Accessed 23 August 2021).
51. K. Moro *et al.*, Ceramide species are elevated in human breast cancer and are associated with less aggressiveness. *Oncotarget* **9**, 19874–19890 (2018).
52. D. Steil *et al.*, Shiga toxin glycosphingolipid receptors of Vero-B4 kidney epithelial cells and their membrane microdomain lipid environment. *J. Lipid Res.* **56**, 2322–2336 (2015).
53. M. I. Khan *et al.*, Comparative gene expression profiling of primary and metastatic renal cell carcinoma stem cell-like cancer cells. *PLoS One* **11**, e0165718 (2016).
54. K. A. Dressler, S. Mathias, R. N. Kolesnick, Tumor necrosis factor- α activates the sphingomyelin signal transduction pathway in a cell-free system. *Science* **255**, 1715–1718 (1992).
55. H. B. Fleit, C. D. Kobasiuk, The human monocyte-like cell line THP-1 expresses Fc γ RI and Fc γ RII. *J. Leukoc. Biol.* **49**, 556–565 (1991).
56. A. V. Kuryagina *et al.*, Plasticity of human THP-1 cell phagocytic activity during macrophagic differentiation. *Biochemistry (Mosc.)* **83**, 200–214 (2018).
57. A. Castoldi *et al.*, Triacylglycerol synthesis enhances macrophage inflammatory function. *Nat. Commun.* **11**, 4107 (2020).
58. C. R. Bollinger, V. Teichgräber, E. Gulbins, Ceramide-enriched membrane domains. *Biochim. Biophys. Acta* **1746**, 284–294 (2005).
59. T. Schramm *et al.*, imzML—A common data format for the flexible exchange and processing of mass spectrometry imaging data. *J. Proteomics* **75**, 5106–5110 (2012).
60. Alexandrovteam, EMBL (2015). pyimzML. <https://github.com/alexandrovteam/pyimzML> (Accessed 17 September 2019).
61. T. Bien, Data from “Mass spectrometry imaging to explore molecular heterogeneity in cell culture.” METASPACE. https://metaspace2020.eu/project/bien_cellular_heterogeneity?tab=datasets. Deposited 27 July 2021.